The combined effect of natural and thermocapillary convection on the melting of phase change materials in rectangular containers

A. Borshchak Kachalov, P. Salgado Sánchez*, J. Porter, J. M. Ezquerro

E-USOC, Departamento de Aeronaves y Vehículos Espaciales, Escuela Técnica Superior de Ingeniería Aeronáutica y del Espacio, Universidad Politécnica de Madrid, Plaza Cardenal Cisneros 3, 28040 Madrid, Spain

Center for Computational Simulation, Universidad Politécnica de Madrid, Campus de Montegancedo, Boadilla del Monte, 28660 Madrid, Spain

Abstract

The results of numerical simulations investigating the influence of natural and thermocapillary convection on the solid/liquid phase transition of n-octadecane in rectangular containers are presented. The melting process is modelled using an enthalpy-porosity formulation of the Navier–Stokes equations. A systematic analysis is performed by varying key dimensionless parameters including the container aspect ratio (Γ), the Rayleigh (Ra) and Marangoni (Ma) numbers, which quantify the strength of natural and thermocapillary convection, and the dynamic Bond number ($\mathrm{Bo}_{\mathrm{dyn}}$), which measures their relative importance. In large containers with $\Gamma \gg 1$ and $\mathrm{Bo}_{\mathrm{dyn}} \ll 1$, thermocapillary convection is shown to significantly accelerate the melting process, enhancing the heat transfer rate of the system by as much as a factor of 20 at large applied Ma. For $\Gamma \lesssim 8$, this enhancement factor takes reduced values of 1–3 and exhibits relatively weak dependence on Ma. In short containers with $\Gamma \lesssim 3$ and $\mathrm{Bo}_{\mathrm{dyn}} \sim O(1)$, the thermocapillary effect is detrimental on average and increases the total melting time. The presence of normal vertical gravity is seen to stabilise the dynamics of the flow, delaying the appearance of oscillatory convection beyond the range of parameters considered here. By reducing $\mathrm{Bo}_{\mathrm{dyn}}$, we examine the transition to microgravity and determine the critical value $\mathrm{Bo}_{\mathrm{dyn}}^{\mathrm{cr}}$ for oscillatory flow at large Ma for the representative aspect ratios 1.5 and 12.

Keywords: Phase Change Materials, Thermocapillary effect, Marangoni convection, Natural convection

1. Introduction

There is a great deal of current interest in energy storage systems that can reduce waste and improve efficiency, an effort motivated in no small part by the worsening environmental problems created by modern society and its immoderate energy consumption habits. Phase change materials (PCMs), which are characterised by their ability to store and release large amounts of thermal energy over a determined temperature range, are an attractive way to control temperature changes and reduce energy loss in a range of applications including air conditioning [1, 2], electronics [3], manufacturing [4, 5] and solar energy [6–9].

The energy storage potential of typical PCMs depends primarily on their heat of fusion, which determines the thermal energy captured during melting and released during solidification. For applications, this heat of fusion should be as large as possible given other material constraints and the need for an appropriate melting temperature T_M. The incorporation of a PCM device increases the thermal inertia of the system and helps maintain its temperature near T_M. A wide assortment of thermal control systems, both passive and active, can be made more efficient with suitable PCM devices.

The potential choices for practical PCMs now cover a wide range of operating temperatures and include both natural and synthetic materials [10, 11]. Among the most commonly used are alkanes, fatty acids and hydrated salts. In particular, organic PCMs like n-octadadecane are largely non-reactive and stable, but are compromised in some applications by their low thermal conductivity, which reduces responsiveness and requires long charge and discharge cycles.

In many situations, the limitations of low conductivity are alleviated in part by natural convection in the liquid, which enhances the total heat transfer rate of the system. A number of different theoretical, numerical and experimental investigations (see, e.g., Refs. [12–18]) were undertaken over the past few decades to determine the role of convection in the melting of PCMs. For example, Beckermann and Viskanta [19] combined ground experiments with numerical simulations to study the melting process in a rectangular container with adiabatic horizontal boundaries and isothermal conditions along the lateral walls. They identified four regimes during the phase change: an initial regime dominated by conduction, a transition regime characterised by developing convection in the upper portion of the container, a convection-dominated regime and one where the melting was strongly influenced by the cold wall.

A rectangular container heated from one side was also considered by Wang et al. [20], who conducted experiments to measure the melting process. They observed the evolution

*Corresponding author
Email address: pablo.salgado@upm.es (P. Salgado Sánchez)

of the solid/liquid interface in detail and reported the temperature distribution along the top and bottom boundaries and the horizontal midplane of the PCM. In contrast to Ref. [19], the melting progressed through three notable regimes: an initial conduction-dominated regime, a transition regime and a convection-dominated one. Transitions were identified via the temporal evolution of the Nusselt number. The absence of the fourth regime of Ref. [19] is likely explained by the different boundary conditions, particularly the temperature and heat flux at the cold wall.

The thermal and heat transport characteristics of the phase change in a mixture of ethanolamine and water was investigated by Yanxia et al. [21]. The melting process was observed in a rectangular container heated through one of the lateral walls and the experiments showed that natural convection accelerates melting compared to the conductive case. The relative importance of the convective flow compared to conduction was characterized by the Rayleigh number (Ra), with higher values leading to a greater difference between the melting rates in the two cases.

A recent review by Dhaidan and Khodadadi [22] examined the influence of the main governing parameters including Ra and the Stefan number (Ste), which characterises the effect of the PCM latent heat, on the phase change process with convection. The influence of container geometry was also considered, from rectangular cavities to spherical capsules and tubes. Central to this comparison is the idea that geometry and orientation can be optimised in order to take advantage of the heat transported by the convective flow in the liquid. Another interesting proposal of this type comes from the work of Gong et al. [23], who suggested inverting the container during the second half of the melting process to encourage more natural convection and potentially improve the heat transfer rate by more than 50%.

Aside from encouraging convective flows, various strategies for increasing heat transport have been proposed that rely on augmenting heat conduction. This can be accomplished, for example, by placing the PCM in contact with more conductive materials (see, e.g., Refs. [24–27]) or by increasing the effective thermal diffusivity of the PCM through the addition of dispersed nanoparticles (see, e.g., Refs. [28, 29]). Note that these solutions involve the incorporation of additional materials, which will generally increase the mass and volume of the thermal control device for a given energy storage capacity.

A special area of application for PCM devices is space exploration, where the microgravity environment of orbiting satellites or the International Space Station precludes the use of natural (buoyant) convection as an additional heat transport mechanism. At the same time, the increase of mass and volume that accompanies most strategies for improving thermal conduction is something to be avoided as much as possible in the space industry. In light of these concerns, the thermocapillary effect was proposed as a mechanism for enhancing heat transfer in microgravity applications. If a free surface is included in the design, then the temperature gradient that accompanies the phase change process will lead to variations in surface tension that will drive thermocapillary convection.

The recent numerical work of Madruga and Mendoza [30, 31] was, to the best of our knowledge, the first to suggest the positive effect of thermocapillary convection on heat transport during the melting of PCMs. These predictions were recently confirmed experimentally by Ezquerro et al. [32, 33], Salgado Sanchez et al. [34], who analysed the effect of thermocapillary flow on the melting of n-octadecane in microgravity conditions. These experiments were the first to quantify the enhancing effect of thermal Marangoni convection on heat transport, with a measured melting rate that was approximately twice that of the case with only thermal diffusion. Prior to these investigations, there were a handful of theoretical studies that considered the influence of the thermocapillary effect on the melting process in microgravity (see, e.g., Refs. [35–38] and references therein).

The relationship between fluid dynamics driven by thermocapillary convection and heat transport was systematically examined by Salgado Sanchez et al. [39, 40] for the melting of n-octadecane in microgravity. The dynamic behaviour of a PCM system is complicated by the fact that the size and geometry of the liquid domain continuously change as the solid/liquid front evolves. Various different flow regimes, which depend on the applied temperatures and the container aspect ratio, were identified and analysed from a bifurcation perspective. Both steady and oscillatory modes — either having the appearance of travelling or (approximately) standing waves — were found, and the critical boundaries between them were determined and discussed in terms of the effective aspect ratio of the liquid domain. The contribution of the thermocapillary effect to the heat transfer rate was quantified and it was seen that, for large containers, heat transport can be enhanced by up to a factor of 20, depending on Marangoni number. For short containers, the enhancement factor was on the order of 5 when oscillatory flow was present.

Given the broad importance of PCM devices in non-space applications, we extend these previous studies here by investigating the combined effect of natural and thermocapillary convection. The principal objective is to identify interesting parameter ranges (i.e., applied temperatures and geometry) for the operation of PCM devices where the thermocapillary effect could be most effectively exploited to improve performance in normal gravity. To the best of our knowledge, only the work of Madruga and Mendoza [30] considered, in a square container, a similar problem. The present work provides a more systematic analysis of parameters.

The manuscript is structured as follows. In Sec. 2, the enthalpy-porosity-based formulation of the Navier–Stokes equations used to model the phase change is presented. In Secs. 3 and 4, respectively, the melting process is described with natural convection and then with the addition of the thermocapillary effect. Section 5 examines the contribution of thermocapillary flow to the heat transfer rate and its effects on melting over a wide range of governing parameters. The influence of gravity is analysed in Sec. 6 from the perspective of heat transport and mode selection, with final conclusions given in Sec. 7.

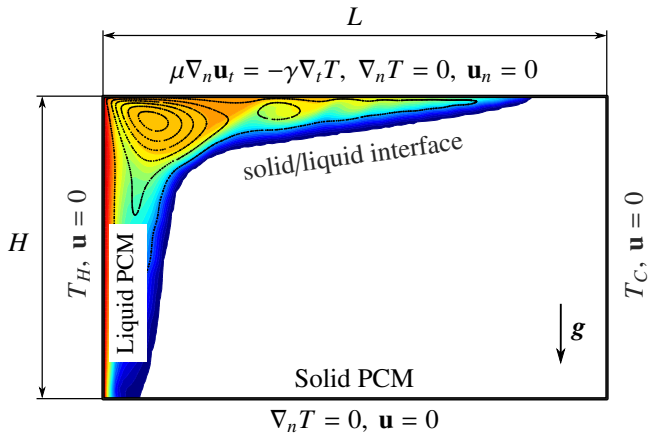

Figure 1: Illustration of the problem considered: a rectangular $L \times H$ volume of n-octadecane (which has a high Prandtl number of 52.53) subjected to constant temperatures T_C and $T_H > T_C$ on opposite lateral walls. The melting process occurs in the presence of constant vertical gravity and a layer of air that bounds the upper surface of the PCM. Once melting begins, there is a liquid/air interface with a temperature gradient that drives thermocapillary convection.

2. Mathematical formulation

We consider a two-dimensional rectangular volume of length L and height H containing a PCM material undergoing a controlled solid/liquid phase transition in the presence of a vertical gravitational field. The melting process is driven by the application of constant temperatures T_C (set here to T_M, the melting temperature) and $T_H > T_C$ on opposite lateral walls. An illustration of this system is provided in Fig. 1.

The phase change occurs in the presence of an air layer that bounds the upper surface of the PCM. The temperature variation along this boundary induces surface tension gradients that drive thermocapillary flow in the liquid. This convection, together with that driven by gravity, provides a mechanism for heat transport and modifies the dynamics of the phase change.

2.1. Governing equations

The Navier–Stokes equations [41] describe the flow in the liquid, which is assumed to be laminar and incompressible. The momentum and mass conservation laws are

$$\rho\left(\frac{\partial \mathbf{u}}{\partial t} + (\mathbf{u}\cdot\nabla)\,\mathbf{u}\right) = -\nabla p + \mu\Delta\mathbf{u} + \rho\mathbf{g}, \tag{1a}$$

$$\nabla\cdot\mathbf{u} = 0, \tag{1b}$$

where $\mathbf{u}$ and p are the velocity and pressure fields, μ is the dynamic viscosity, ρ is the density, and $\mathbf{g}$ is the vertically-oriented gravitational acceleration; its magnitude will be characterised by $g = |\mathbf{g}|/g_0$ where $g_0 = 9.81\,\mathrm{m/s^2}$.

The conservation of thermal energy encompasses temperature changes (sensible heat) and the phase change (latent heat):

$$\rho c_p\left(\frac{\partial T}{\partial t} + \mathbf{u}\cdot\nabla T\right) = k\Delta T - \rho c_L\left(\frac{\partial f}{\partial t} + \mathbf{u}\cdot\nabla f\right), \tag{2}$$

where T is the temperature field, c_p is the specific heat capacity at constant pressure, k is the thermal conductivity, c_L is the latent heat, and f is the liquid fraction defined below.

During melting, the heat of fusion depends on the quantity of melted material via the expression $f\rho\,c_L$. This product couples the energy and momentum equations through the (local) liquid fraction f, which can be written as a temperature-dependent field. This dependence is modelled in this work using a smoothed step (Heaviside) function:

$$f(T) = \begin{cases} 0 & \widetilde{T} < -\delta_T/2, \\ \frac{1}{2} + \frac{\widetilde{T}}{2\delta_T} + \frac{1}{2\pi}\sin\left(\frac{\pi\widetilde{T}}{\delta_T}\right) & |\widetilde{T}| \le \delta_T/2, \\ 1 & \widetilde{T} > \delta_T/2, \end{cases} \tag{3}$$

where $\widetilde{T} = T - T_\mathrm{M}$. This function changes from 0 to 1 near the phase change temperature T_M across the interval δ_T, which characterises the so-called "mushy region" where solid and liquid phases may coexist [42].

The PCM is treated continuously by making all physical properties dependent on T with appropriate limits for the solid and liquid phases. These are expressed using the liquid fraction f as follows:

$$\rho = \rho_\mathrm{S} + (\rho_\mathrm{L} - \rho_\mathrm{S})f, \tag{4a}$$

$$\mu = \mu_\mathrm{S} + (\mu_\mathrm{L} - \mu_\mathrm{S})f, \tag{4b}$$

$$c_p = c_{p\mathrm{S}} + (c_{p\mathrm{L}} - c_{p\mathrm{S}})f, \tag{4c}$$

$$k = k_\mathrm{S} + (k_\mathrm{L} - k_\mathrm{S})f, \tag{4d}$$

where the subscripts L and S denote liquid and solid, respectively.

Due to (small) variations of the liquid density with temperature, the presence of gravity induces natural convection in the liquid phase. We assume a linear dependence of ρ_L on T:

$$\rho_\mathrm{L} = \rho_0\left[1 - \beta(T - T_M)\right], \tag{5}$$

where ρ_0 is the density value at the melting (reference) temperature T_M and β is the thermal expansion coefficient.

The parameter μ_S denotes a virtual solid viscosity, which is taken several orders of magnitude greater than μ_L so that the velocity is effectively zero in the solid [43]. We select a value of $\mu_\mathrm{S} = 10^3$ Pa s in accord with Refs. [34, 39, 40].

2.2. Boundary conditions

The thermocapillary effect is modelled with a linear dependence of interfacial tension on temperature,

$$\sigma = \sigma_0 - \gamma\,(T - T_M)\,. \tag{6}$$

Here, σ_0 denotes the surface tension at temperature T_M, while the thermocapillary coefficient $\gamma = -\partial\sigma/\partial T$ characterises its derivative at that point. The variation of σ with T produces a tangential force that draws fluid along the interface from regions of lower to higher σ, thereby driving thermocapillary flow. In the solid phase ($T \le T_M$), we impose $\gamma = 0$.

At the thermocapillary (liquid/air) interface, there is generally a balance between pressure, viscous stress and surface tension. In this formulation, we assume a perfectly flat interface so that the only effect of surface tension is through γ and the force balance reduces to

$$\mu\nabla_n\mathbf{u}_t = -\gamma\nabla_t T, \tag{7}$$

where the subscripts n and t refer to the normal and tangential components, respectively.

The main error in neglecting the curvature of the interface is related to the thermal expansion that occurs during the transition from solid to liquid, which is inconsistent with a fixed rectangular domain. However, the recent work of Salgado Sanchez et al. [34] on the melting of n-octadecane found good agreement between experiments and numerical simulations in rectangular geometry, which provides some justification for this simplifying assumption. In similar fashion, the free surface deformation caused by the thermocapillary flow is expected to be negligible, consistent with results obtained by Montanero et al. [44] and Shevtsova et al. [45]. This deformation was shown to be proportional to the capillary number $\mathrm{Ca} = \gamma \Delta T/\sigma_0$. In the case of n-octadecane, $\sigma_0 \simeq 27.54\,\mathrm{mN/m}$ and $\gamma = 8.44 \times 10^{-5}\,\mathrm{N/(m\,K)}$ (see Table 1) while the temperature interval considered here is $\Delta T = T_H - T_M \leq 40\,\mathrm{K}$. Thus, $\mathrm{Ca} \leq 0.12$ and the expected deformation is on the order of micrometers.

The remaining boundary conditions (also indicated in Fig. 1) are as follows:

– Along the lateral walls:

$$T = T_H,\ T_C; \quad \mathbf{u} = 0, \tag{8}$$

where $T_H = T_M + \Delta T$ and $T_C = T_M$.

– Along the bottom wall:

$$\nabla_n T = 0; \quad \mathbf{u} = 0. \tag{9}$$

– Along the free surface, Eq. (7) is enforced and

$$\nabla_n T = 0; \quad \mathbf{u}_n = 0. \tag{10}$$

2.3. Scaling and governing parameters

We scale distance by L, so that $x \in [0, 1]$ and $y \in [0, 1/\Gamma]$ are dimensionless horizontal and vertical coordinates, respectively, with the container aspect ratio

$$\Gamma = \frac{L}{H}. \tag{11}$$

The characteristic timescale is taken to be that of thermal diffusion in the liquid,

$$\tau = t\,\frac{\alpha}{L^2}\,, \tag{12}$$

where $\alpha = k_\mathrm{L}/(\rho_0\, c_{p\mathrm{L}})$ is the liquid thermal diffusivity. Temperature relative to T_M is scaled with the applied difference $T_H - T_M$:

$$\Theta = \frac{T - T_M}{T_H - T_M}\,. \tag{13}$$

With the physical properties of the liquid as reference values for density, viscosity, thermal conductivity and heat capacity at constant pressure, the dynamics of Eqs. (1)–(10) are characterised by the ratios of these properties between solid and liquid,

$$\widetilde{\rho} = \frac{\rho_\mathrm{S}}{\rho_0}, \quad \widetilde{\mu} = \frac{\mu_\mathrm{S}}{\mu_\mathrm{L}}, \quad \widetilde{k} = \frac{k_\mathrm{S}}{k_\mathrm{L}}, \quad \widetilde{c_p} = \frac{c_{p\mathrm{S}}}{c_{p\mathrm{L}}}, \tag{14}$$

and by the Marangoni number,

$$\mathrm{Ma} = \frac{\gamma\, L\, \Delta T}{\mu_\mathrm{L}\alpha}, \tag{15}$$

the Stefan number

$$\mathrm{Ste} = \frac{c_{p\mathrm{L}}\Delta T}{c_L}, \tag{16}$$

the Rayleigh number,

$$\mathrm{Ra}_L = \frac{g\,\rho_0\, g_0 \beta\, L^3\, \Delta T}{\mu_\mathrm{L}\alpha}, \tag{17}$$

the Prandtl number,

$$\mathrm{Pr} = \frac{\mu_\mathrm{L}}{\rho_0\,\alpha}, \tag{18}$$

and the aspect ratio Γ.

The PCM n-octadecane is selected here for to its relevance to recent microgravity experiments [32–34]. The physical properties of this material are listed in Table 1, from which one obtains the nondimensional parameters

$$\mathrm{Pr} = 52.53, \quad \widetilde{\rho} = 1.11, \quad \widetilde{k} = 2.42, \quad \widetilde{c_p} = 0.88. \tag{19}$$

Note that the assumption of two-dimensional dynamics is consistent with the behaviour of high Pr fluids [46–48].

We find it convenient to rescale the Rayleigh number with the height of the container H;

$$\mathrm{Ra} = \mathrm{Ra}_L\,\Gamma^{-3}, \tag{20}$$

and use the dynamic Bond number,

$$\mathrm{Bo}_\mathrm{dyn} = \frac{\mathrm{Ra}}{\mathrm{Ma}} = \frac{g\,\rho_0\, g_0 \beta\, H^2}{\gamma\,\Gamma}, \tag{21}$$

to quantify the relative importance of buoyancy and the thermocapillary effect.

Melting temperature, T_M	28 °C
Liquid density (ref.), ρ_0	$780\,\mathrm{kg/m^3}$
Solid density, ρ_S	$865\,\mathrm{kg/m^3}$
Specific latent heat, c_L	$243.5\,\mathrm{kJ/kg}$
Liquid specific heat capacity, $c_{p\mathrm{L}}$	$2196\,\mathrm{J/(kg\,K)}$
Solid specific heat capacity, $c_{p\mathrm{S}}$	$1934\,\mathrm{J/(kg\,K)}$
Liquid conductivity, k_L	$0.148\,\mathrm{W/(m\,K)}$
Solid conductivity, k_S	$0.358\,\mathrm{W/(m\,K)}$
Dynamic viscosity, μ_L	$3.541 \times 10^{-3}\,\mathrm{Pa\,s}$
Thermal expansion coefficient, β	$9.1 \times 10^{-4}\,\mathrm{1/K}$
Thermocapillary coefficient, γ	$8.44 \times 10^{-5}\,\mathrm{N/(m\,K)}$

Table 1: Physical properties of n-octadecane, reproduced from [34].

2.4. Numerical approach

The governing equations (1)–(7) together with the boundary conditions (8)–(10) are solved in COMSOL Multiphysics (using dimensional variables) with the finite element method. As in Refs. [39, 40], the initial temperature throughout the PCM is set to 25 °C and, since the PCM is solid for $T < T_M$, the initial velocity is $\mathbf{u} = 0$. The initial temperature profile leads to a sharp jump (mismatch) at the hot and cold boundaries that is treated numerically by taking the first time step with a backward Euler method [40].

The evolution is calculated using a backward differentiation formula scheme with maximum time steps $\Delta t \in [0.0001, 0.01]$ s that depend on the applied temperatures and are selected to satisfy the Courant–Friedrichs–Lewy convergence condition. Streamline [49] and crosswind [50] stabilisation techniques are implemented to avoid spurious numerical oscillations.

Further details of the numerical simulations can be found in Refs. [34, 39, 40]. Below, we summarise the convergence tests used to select the maximum mesh size.

2.4.1. Mesh selection and numerical convergence

As in Refs. [39, 40], we use the melting time τ_{melt} at which the PCM is 100% liquid as an indicative value for testing numerical convergence.

The results of simulations using different meshes with only natural convection are shown in Table 2(a,b) for an applied temperature difference $\Delta T = 25$ K with $\Gamma = 1.5$ and $\Gamma = 12$, respectively. Note that, since $L = 0.0225$ m in both cases while H is varied, the nondimensional parameter Ra_L remains constant in (a) and (b). Each of the mesh choices is characterised by the maximum element size (as a fraction of the container length L), the melting time τ_{melt} and the deviation of this time from that obtained with the most refined mesh. The mesh selections a2 and b1 (marked in bold) are found to provide acceptable numerical accuracy.

The results of simulations with combined natural and thermocapillary convection are given in the same manner in Table 2(c,d). The deviation of τ_{melt} is less than 5% for the selected mesh c2 (marked in bold), while it is less than 1% for mesh d1.

Although more refined meshes than those selected in (b) and (c) could arguably be used, we find, as in the related numerical investigations of Salgado Sanchez et al. [39, 40], that they offer a reasonable compromise between numerical accuracy and computational cost. In the remainder of this work, the maximum mesh size is set to $\mathcal{S} = L/67.5$ if $\Gamma < 4.5$ and $(3/4)\mathcal{S}$ if $\Gamma \geq 4.5$. These selections are also consistent with the recent work of Salgado Sanchez et al. [34] where numerical simulations using a similar mesh size were validated against experiments.

Natural convection (g)

(a) $\Gamma = 1.5$, $\text{Ra} = 1.9205 \times 10^6$

Mesh #	Max. size ($\times L/67.5$)	τ_{melt}	Deviation (%)
a1	3/2	0.5233	−4.37
a2	**1**	**0.5434**	**−0.69**
a3	3/4	0.5472	—

(b) $\Gamma = 12$, $\text{Ra} = 3751$

Mesh #	Max. size ($\times L/67.5$)	τ_{melt}	Deviation (%)
b1	**3/4**	**0.8418**	**−3.47**
b2	1/4	0.8346	—

Natural + thermocapillary convection (g + Ma)

(c) $\Gamma = 1.5$, $\text{Ma} = 155186$

Mesh #	Max. size ($\times L/67.5$)	τ_{melt}	Deviation (%)
c1	3/2	0.7503	8.01
c2	**1**	**0.7261**	**4.52**
c3	3/4	0.6946	—

(d) $\Gamma = 12$, $\text{Ma} = 155186$

Mesh #	Max. size ($\times L/67.5$)	τ_{melt}	Deviation (%)
d1	**3/4**	**0.1045**	**0.86**
d2	1/4	0.1082	—

Table 2: Results of mesh convergence tests in normal gravity ($g = 1$): (a, b) Simulations with only natural convection in containers with (a) $\Gamma = 1.5$, (b) $\Gamma = 12$; (c, d) simulations with combined thermocapillary and natural convection in containers with (c) $\Gamma = 1.5$, (d) $\Gamma = 12$. Comparison between meshes is made in terms of the deviation of the melting time τ_{melt} with respect to the finest mesh. The selected meshes a2, b1, c2 and d1 are marked in bold.

3. Melting with natural convection

This section considers the phase change process with only natural convection. The results are also used below for comparing heat transfer rates when the thermocapillary effect is included. Since, without the thermocapillary effect, the only source of fluid motion is buoyancy due to density variations in the liquid, the problem can be described by the formulation of Sec. 2 with $\gamma = 0$. In this case, the (nonconstant) governing parameters are Ste, Ra, and Γ.

In the manner of previous work [39, 40], we conduct a systematic parametric study of the melting dynamics by varying the applied temperature difference (Ste and Ra) and the container geometry (Γ and Ra). Representative cases are used to illustrate the dynamics of melting in different regimes. The related discussion focusses on a long container with $\Gamma = 12$ and a short one with $\Gamma = 1.5$, and on two applied Ra (Ste) numbers.

The phase change process in long containers is illustrated in Fig. 2 for $\Gamma = 12$. Two sets of results are shown for (a) $\text{Ra} = 750$ and (b) $\text{Ra} = 4501$, which correspond to $\Delta T = 5$ K and $\Delta T = 30$ K, respectively. The colourmap (cold in blue,

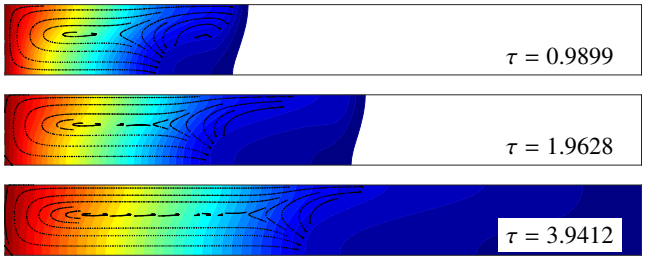

(a) Ra = 750

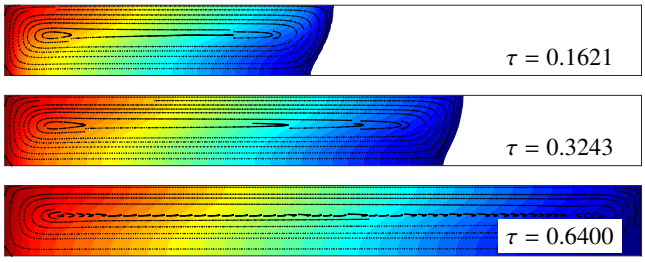

(b) Ra = 4501

Figure 2: Snapshots (times indicated) showing the evolution of the melting PCM with natural convection for $\Gamma = 12$ and different applied temperatures: (a) Ra = 750 ($\Delta T = 5$ K), (b) Ra = 4501 ($\Delta T = 30$ K). The colourmap shows the temperature field Θ (warm in red, cold in blue) with streamlines of the flow (black curves) superimposed. The PCM is completely melted by $\tau_{\text{melt}} = 3.9412$ in (a) and $\tau_{\text{melt}} = 0.6400$ in (b). For both Ra, the flow is characterised by a large vortex that extends throughout the liquid.

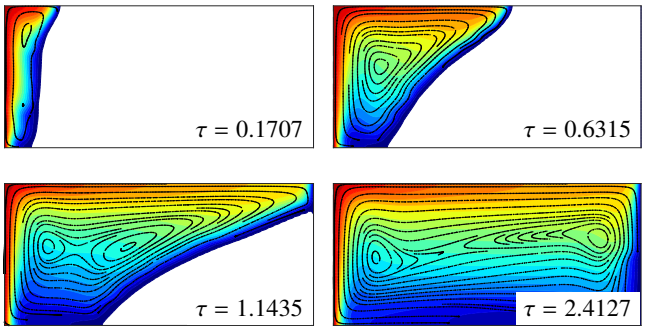

(a) Ra = 3.8409×10^5

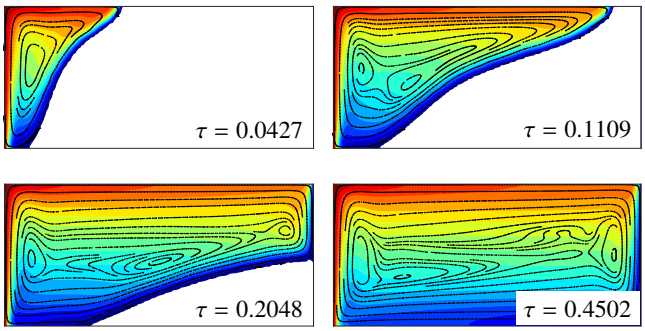

(b) Ra = 2.3046×10^6

Figure 3: Snapshots (times indicated) showing the evolution of the melting PCM with natural convection for $\Gamma = 1.5$ and different applied temperatures: (a) Ra = 3.8409×10^5 ($\Delta T = 5$ K), (b) Ra = 2.3046×10^6 ($\Delta T = 30$ K). The colourmap shows the temperature field $\Theta = 1$ (warm in red, cold in blue) with streamlines of the flow (black curves) superimposed. The PCM is completely melted by $\tau_{\text{melt}} = 2.4127$ in (a) and $\tau_{\text{melt}} = 0.4502$ in (b). For both Ra, the final flow is characterised by a (nearly antisymmetric) structure of two vortices centred at the vertical midline of the container.

warm in red) shows the dimensionless temperature field Θ in the liquid, with streamlines of the flow superimposed on this.

The dynamics in both cases is qualitatively similar, except for the reduction in melting time from $\tau_{\text{melt}} = 3.9412$ to $\tau_{\text{melt}} = 0.6400$ with the higher Ra (Ste). The presence of natural convection in the liquid is revealed not only by the streamlines but by the curvature of the isotherms. The fact that this convection draws warmer liquid towards the upper part of the container results in slightly faster melting in this region, as revealed by the inclination of the solid/liquid front. With higher Ra (Ste), the convective motion is stronger and the inclination is correspondingly greater.

With both Ra (Ste) numbers, the flow in the liquid is similar to the classical *steady return flow* (SRF) solution [51], which is characterised by a large vortex extending throughout the liquid, but centred near the horizontal midline of the container. With Ra = 750, there is a notable distortion of these streamlines in the vicinity of the cold boundary (either at the solid/liquid front or the cold wall) due to the effect of the mushy region and the transition between the liquid and solid viscosities [39]. With the larger applied temperature difference of Ra = 4501, the influence of the mushy region is diminished and restricted to a thin layer near the cold side; it is not noticeable on the scale of the figure.

In Ref. [40], the melting process of n-octadecane was analysed in microgravity with only thermal diffusion. In that case, the respective melting times for the same $\Delta T = 5$ K (Ste = 0.045) and $\Delta T = 30$ K (Ste = 0.271) were $\tau_{\text{melt}} = 7.1470$ and $\tau_{\text{melt}} = 1.8638$; values of Ste are reported here since Ra = 0 in microgravity. A comparison of melting times shows that natural convection enhances the average heat transfer rate by factors of 1.81 and 2.91, respectively, which is consistent with the observations of Yanxia et al. [21].

The melting process in short containers is illustrated with $\Gamma = 1.5$ in Fig. 3 for (a) Ra = 3.8409×10^5 ($\Delta T = 5$ K) and (b) Ra = 2.3046×10^6 ($\Delta T = 30$ K). Note that these Ra values are substantially bigger than those of Fig. 2 because they scale (for fixed length L) with Γ^{-3} [see Eq. (20)]. The colourmap shows the dimensionless temperature field Θ with streamlines superimposed.

Again, the melting dynamics are similar for both Ra values. At the beginning of the phase change process, heat transport is dominated by diffusion and both the solid/liquid front and the isotherms are aligned (approximately) vertically [40]. When the solid/liquid front separates enough from the hot boundary, gravity and natural convection come into play, generating a large vortex that pulls hot liquid towards the upper part of the cell and, thus, accelerates the melting there; see panels (a) at $\tau = 0.1707$ and (b) at $\tau = 0.0427$. This uneven melting persists during the advance of the solid/liquid front, until it reaches the cold wall. Beyond that, the evolution of the solid/liquid front can only proceed downwards. As discussed in Refs. [19, 20],

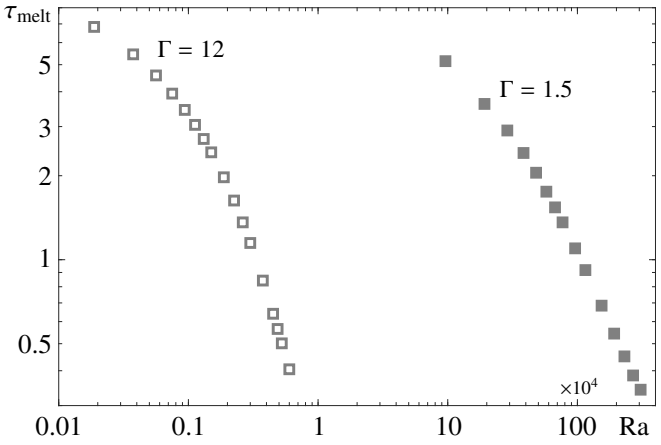

Figure 4: Melting time τ_{melt} with natural convection in containers of $\Gamma = 12$ (open squares) and $\Gamma = 1.5$ (solid squares) as a function of Ra. Note the logarithmic scale of the axes.

a series of regimes can be distinguished as melting progresses. The first is dominated by conduction, the second by developing convection in the upper portion of the PCM, and the third by fully-developed convection. The fourth is strongly influenced by the cold wall and its thermal boundary conditions.

The flow in the liquid transforms from an initial large vortex to a final structure with two vortices centred near the lateral walls and approximately halfway up. This final state, with the PCM completely melted, is that of a simple liquid differentially heated from the sides. The fact that the thermal gradient is applied horizontally while the gravitational force is vertical means that neither left-right nor up-down symmetry is expected; this asymmetry is evident in both the temperature field and the streamlines. We note that the proximity of the vortices to the solid/liquid front during the latter stage seems to be effective in increasing the melting rate; this observation will be discussed in more detail below.

Comparing these results with the case of microgravity and purely diffusive heat transfer [40], we find that the melting times are reduced by factors of 2.96 and 4.13, respectively, which are significantly larger than the factors obtained for $\Gamma = 12$. This reflects the enhanced effect of gravity in deeper containers and the natural convection it induces, which is indicated by larger Ra [21].

Figure 4 shows the results of extending this investigation over a wide interval of Ra. The melting time τ_{melt} is obtained as a function of Ra and displayed on a logarithmic scale. As expected, τ_{melt} decreases with Ra [21], and appears to follow a regular scaling law for large values. In the limit of small Ra (Ste), the change in scaling is largely explained by the mushy region (i.e., the fact that the phase change occurs over a finite interval δ_T of temperatures), consistent with Ref. [40].

4. Melting with natural and thermocapillary convection

Here, the phase change transition is studied under the combined effect of natural and thermocapillary convection. As in Sec. 3, we conduct a systematic parametric study of the melting

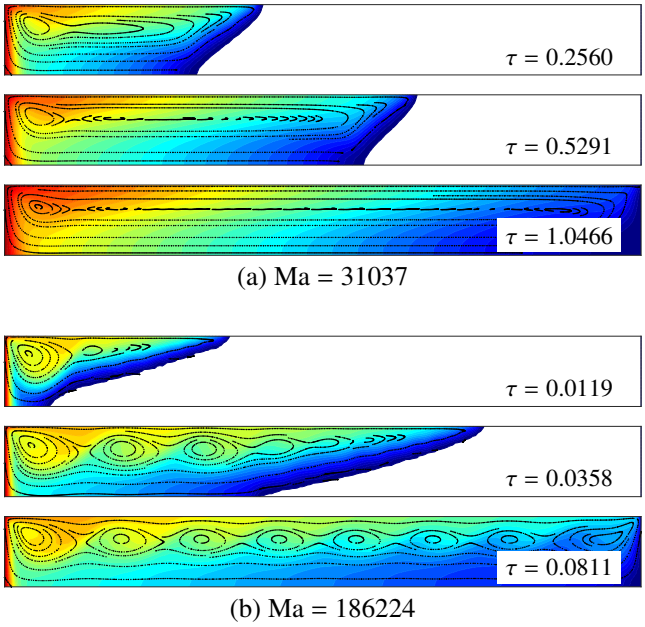

Figure 5: Snapshots (times indicated) showing the evolution of the melting PCM with both natural and thermocapillary convection for $\Gamma = 12$ and (a) Ma = 31037 ($\Delta T = 5$ K), (b) Ma = 186224 ($\Delta T = 30$ K). The colourmap shows the temperature field Θ (warm in red, cold in blue) with streamlines of the flow (black curves) superimposed. The PCM is completely melted by $\tau_{melt} = 1.0466$ in (a) and $\tau_{melt} = 0.0811$ in (b). Depending on Ma, the flow is characterised by vortices forming (a) *steady return flow* or (b) a *steady multicellular structure* (SMC). Note the vertical alignment of the structure at approximately $2H/3$ in both cases.

dynamics by varying the applied temperature difference (Ma, Ste and Ra) and the aspect ratio Γ. Representative cases are used to illustrate the dynamics of melting in different regimes. In particular, results are discussed for two Ma values in a long container with $\Gamma = 12$ and in a short container with $\Gamma = 1.5$.

Figure 5 depicts the melting process in a large container for (a) Ma = 31037 and (b) Ma = 186224. The colourmap shows the dimensionless temperature field Θ with the streamlines of the flow superimposed. Note that the Ra values for these simulations are as in Fig. 2, which can be directly compared.

The fact that the Ra values are small compared to the Ma values indicates the diminishing importance of gravitational effects relative to thermocapillary effects; this is quantified by $\mathrm{Bo}_{dyn} \simeq 0.024 \ll 1$, which is independent of ΔT [see Eq. (21)]. The melting process for low Bo_{dyn} can be expected to resemble that of the microgravity case in some respects. In particular, the features of the flow in (a) recall the SRF solution and those in (b) the *steady multicellular structure* (SMC) discussed in Ref. [39], with the characteristic vertical alignment of the cells near $2H/3$. In contrast to that study, where a critical Ma of $\mathrm{Ma}_{cr} = 97660$ ($\Delta T = 15.73$ K) for oscillatory thermocapillary flow was determined, the melting process at large Ma remains (quasi-) steady in the presence of natural convection over the range of parameters explored here: Ma ≤ 248298 ($\Delta T \leq 40$ K). The observed stabilising effect of gravity, which delays the appearance of oscillatory thermocapillary flow, is consistent with the work of Shevtsova et al. [52], where an extensive analysis

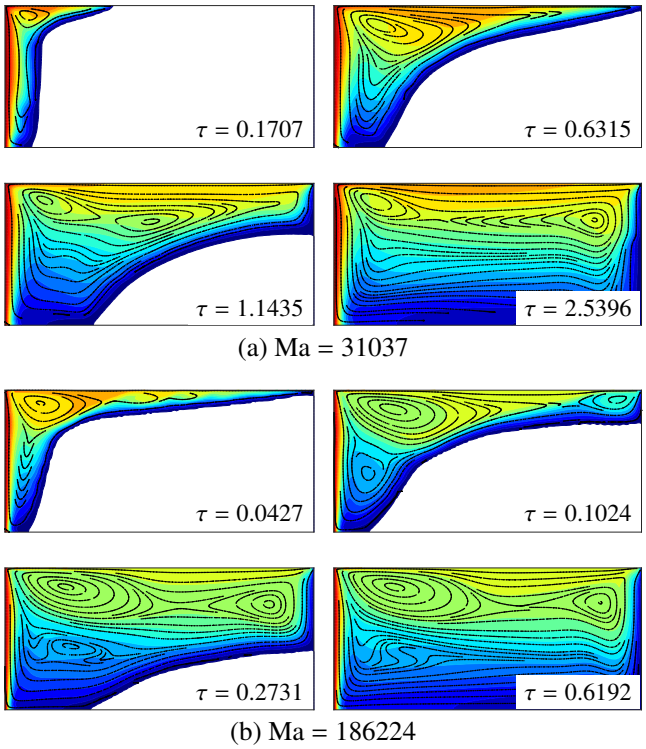

Figure 6: Snapshots (times indicated) showing the evolution of the melting PCM with both natural and thermocapillary convection for $\Gamma = 1.5$ and (a) Ma = 31037 ($\Delta T = 5\,\mathrm{K}$), (b) Ma = 186224 ($\Delta T = 30\,\mathrm{K}$). The colourmap shows the temperature field Θ (warm in red, cold in blue) with streamlines of the flow (black curves) superimposed. The PCM is completely melted by $\tau_{\mathrm{melt}} = 2.5396$ in (a) and $\tau_{\mathrm{melt}} = 0.6192$ in (b). In both cases, the flow is characterised by a pair of vortexes located close to the free surface. For the higher Ma, a transient SMC appears during the early part of the melting in the thin thermocapillary layer near this free surface.

of thermocapillary-buoyant convection in a large container of $\Gamma \simeq 24$ was conducted over the range $0 < \mathrm{Bo_{dyn}} < 0.8$.

The measured melting times are $\tau_{\mathrm{melt}} = 1.0466$ for Ma = 31037 and $\tau_{\mathrm{melt}} = 0.0811$ for Ma = 186224. The enhancement factors with respect to the case of only natural convection are 3.7657 and 7.8915, respectively, which shows the substantial benefit to heat transport in PCMs that thermocapillary flow can provide — beyond the improvement already provided by natural convection. The idea of combining the thermocapillary effect with other strategies to enhance PCM performance has been recently discussed in Ref. [53].

In addition to its effect on τ_{melt}, the applied Ma is important in selecting the number of vortices within the SMC. At the onset of the SMC mode, the SRF structure splits into a pair of vortices that spread outwards from the hot wall. As Ma is increased, the number of vortices observed in the SMC first increases as well, but eventually saturates. In fact, while eight vortices are seen in Fig. 5(b) at $\tau = 0.0811$, further increase to Ma = 248298 (a simulation not included here) results in a final structure with only seven vortices.

The melting process for a short container of $\Gamma = 1.5$ is illustrated in Fig. 6 for the same values of (a) Ma = 31037 and (b) Ma = 186224. The snapshots show the temperature field in

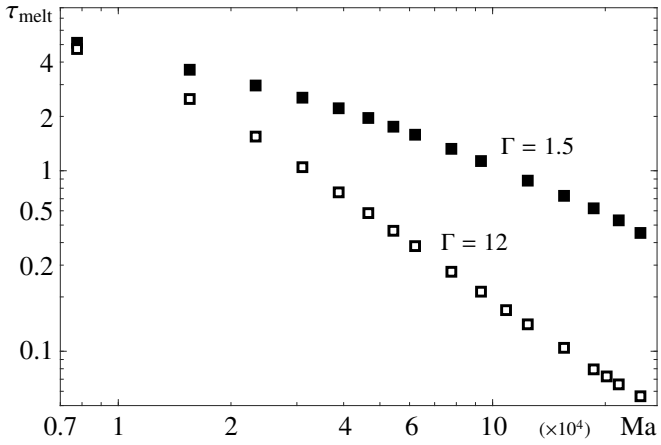

Figure 7: Melting time τ_{melt} with both natural and thermocapillary convection in containers of $\Gamma = 12$ (open markers) and $\Gamma = 1.5$ (solid markers) as a function of Ma. Note the logarithmic scale of the axes.

the liquid (using a colourmap) and the streamlines of the flow. Note that the associated Ra values are as in Fig. 3, which can be directly compared. Here, $\mathrm{Bo_{dyn}} \simeq 12.38$, which reflects the increasing importance of buoyancy in deep (small Γ) containers.

For both Ma values, the melting dynamics are similar to that of Sec. 3, except for accelerated melting near the thermocapillary surface. With Ma = 31037, in particular, the solid/liquid front clearly reaches the cold wall faster than it does without the thermocapillary effect, as observed at $\tau = 0.6315$ (see Fig. 3 for comparison). Another consequence of thermocapillary flow is that the final vortices are displaced towards the free surface; with only natural convection, they are centred vertically near the midline.

With larger Ma, as in Fig. 6(b), the differences with respect to only natural convection are even more evident, especially the faster melting near the free surface (see the snapshot at $\tau = 0.0427$). As discussed in Refs. [39, 40], this thin layer of liquid experiences an effective aspect ratio Γ_{eff} that is larger than Γ. This fact explains the transient appearance of a flow structure with multiple vortices resembling the SMC. As soon as the solid/liquid front reaches the cold wall, the value of Γ_{eff} decreases and the number of vortices in the structure does too. The final state contains two vortices, with the strongest flow shifted towards the thermocapillary surface and the hot boundary.

The melting dynamics are (quasi-) steady in the presence of normal gravity, at least over the range Ma $\leq$ 248298 ($\Delta T \leq 40\,\mathrm{K}$) considered here. This is in contrast to the microgravity results of Salgado Sanchez et al. [39], where modulated thermocapillary flow appears in the form of an *oscillatory standing wave* (OSW) mode for these same parameters. This difference is an additional evidence of the stabilising effect of gravity on thermocapillary convection. In this case, since $\mathrm{Bo_{dyn}}$ is substantially larger than for long containers, the delay of the critical Ma is expected to be larger as well, as shown in Ref. [52].

The melting times for the Ma values of Fig. 6 are $\tau_{\mathrm{melt}} = 2.5396$ in (a) and $\tau_{\mathrm{melt}} = 0.6192$ in (b). Compared to the case

of only natural convection, heat transport is reduced by factors of 0.9500 and 0.7271, respectively, which shows that the thermocapillary effect can delay melting for $\Gamma = 1.5$. Some explanation for this can be be found in the structure of the flow. In Sec. 3, the vortices are centred near the vertical midline of the container, which allows them to more effectively transport heat during the later stage of the melting process when the solid portion of PCM recedes downwards. While the presence of the thermocapillary effect accelerates melting during the earlier part of the phase change process, it also shifts the centres of the vortices upwards, which reduces their influence on the solid/liquid front at later times. This detrimental effect on the overall melting process will be discussed in more detail below.

To complete the analysis, we measure τ_{melt} after varying ΔT to cover the range $0 < \text{Ma} \leq 248298$. These melting times are shown in Fig. 7 for $\Gamma = 12$ (open markers) and $\Gamma = 1.5$ (solid markers); note the logarithmic scale. The general tendency, as expected, is for τ_{melt} to decrease with Ma. At lower Ma, a change of scaling similar to that seen in Sec. 3 and Ref. [40] is apparent. As mentioned, this is inherent to the enthalpy-porosity formulation used to solve the phase change and the extent of the mushy region. There is no evidence of a change in scaling for large Ma, which stands in contrast to the microgravity case studied in Ref. [40], where the appearance of oscillatory modes has a noticeable effect on heat transport. As noted above, the flow here is always (quasi-) steady.

5. Quantification of heat transport during melting

In this section, we measure the contribution of thermocapillary convection to the overall heat transport during the phase change process with normal gravity. The effect is quantified by the ratio of melting times with only natural convection to that with mixed natural and thermocapillary convection.

Figure 8 summarises the results obtained over a wide range of Ma values and $1.5 \leq \Gamma \leq 24.7$. The enhancement factor is defined as

$$\mathcal{G} = \frac{\tau_{\text{g}}}{\tau_{\text{g+Ma}}}, \tag{22}$$

where the subscripts "g" and "g + Ma" refer to natural convection, and to combined natural and thermocapillary convection, respectively. Data points from the simulations are marked (open squares) and interpolated to estimate the continuous contours (dashed curves). These are labelled by the corresponding enhancement factor $\mathcal{G}$, with the neutral contour $\mathcal{G} = 1$, where $\tau_{\text{g}} = \tau_{\text{g+Ma}}$, distinguished by a solid curve. Note that in the limit $\text{Ma} \to 0$ the factor $\mathcal{G}$ is close to unity [40]. For finite Ma, the thermocapillary contribution leads to a range of $\mathcal{G}$ values between approximately 0.7 and 20, which can be separated into three qualitatively different regimes depending largely on Γ.

For long containers with $\Gamma \gtrsim 17$, there is strong dependence of $\mathcal{G}$ on Ma. Indeed, it is here that the enhancement factor reaches values of up to 20 at large Ma. This regime is associated with shallow containers characterised by $\text{Bo}_{\text{dyn}} \ll 1$ where convective flow is primarily due to the thermocapillary effect.

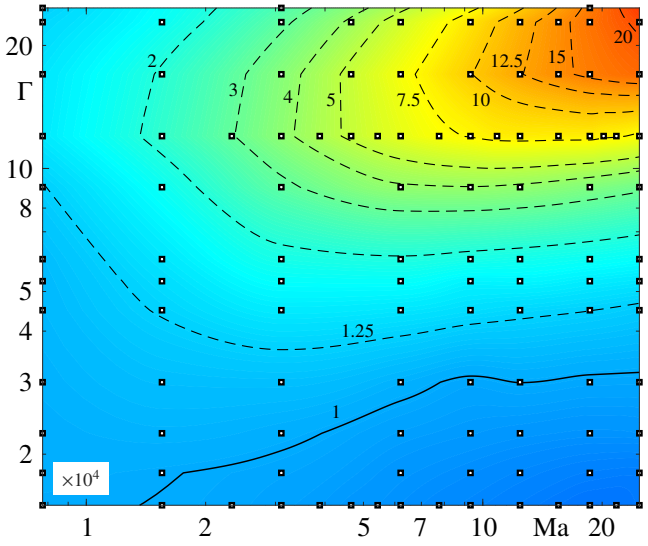

Figure 8: Contours of the enhancement factor $\mathcal{G}$ (dashed curves with labelled values) for varying Ma and Γ. The neutral case of $\mathcal{G} = 1$ is distinguished by a thicker solid curve. The data points obtained from the simulations are marked with open squares.

For large enough Ma, the enhancing effect of thermocapillary flow saturates, consistent with the results of Ref. [40].

In the case of short containers with $\Gamma \lesssim 8$, the enhancement factor $\mathcal{G}$ is substantially smaller than with larger Γ. Indeed, for $\Gamma \lesssim 3$, an increase in Ma actually reduces $\mathcal{G}$ and, thus, the performance of the PCM. An explanation for this was given above in terms of the proximity of the vortical structure to the thermocapillary surface. This upward shift of the vortices compared to the more centred structures observed with only natural convection makes them less effective at transferring heat downwards and leads to slower melting during the final stage of the process. The contours of $\mathcal{G}$ are relatively flat in this regime, indicating weak dependence on Ma. Depending on the application, this fact could be seen as an advantage, since a PCM design with $3 \lesssim \Gamma \lesssim 8$ would have an enhancement factor of approximately 1.25–3 over a wide range of operating temperatures.

In the intermediate regime with $8 \lesssim \Gamma \lesssim 17$, the behaviour of $\mathcal{G}$ is more varied. For low Ma values, an increase in thermal forcing leads to a clear rise in $\mathcal{G}$. This dependence weakens, however, for large Ma values where the contours become relatively flat.

Finally, an important implication of Fig. 8 is that for a given Ma, the enhancement factor $\mathcal{G}$ takes a maximum value at finite Γ. This behaviour, also identified in Ref. [40], means that there is an optimal curve $\Gamma(\text{Ma})$ locating the aspect ratio that maximises thermocapillary enhancement. The fact that $\mathcal{G}$ declines beyond this optimal Γ is related to the loss of momentum as H becomes comparable to the thickness of the boundary layers. In this limit, the fluid motion is affected by increased drag, which reduces convection and the heat transport associated with it.

6. Influence of dynamic Bond number

By comparing the results of Secs. 3–5 to previous microgravity studies [39, 40], we can identify the main differences in the melting behaviour found with PCMs under normal gravity. These differences, which refer to heat transport properties as well as mode selection in the flow, are summarised by the following points.

1. In short containers, the enhancement factor $\mathcal{G}$ is $O(1)$ and shows weak dependence on Ma. The thermocapillary effect can even be detrimental to average heat transport during melting, increasing τ_{melt}.
2. In long containers, the effect of natural convection is weak, and results are similar in some ways to those in microgravity. The enhancement factor $\mathcal{G}$ can reach values as high as 20 for large Ma.
3. The presence of natural convection has a stabilising effect on the dynamics of the flow. Steady convection modes are found over the entire range of parameters explored here. This is in contrast to weightless environments, where either the *hydrothermal travelling wave* (HTW) or the OSW modes are found beyond a critical Ma, depending on Γ.

In this section, we analyse the transition from normal gravity to microgravity by varying the dynamic Bond number Bo_{dyn}. Particular choices of gravitational acceleration include those of the Moon ($g = 0.1651$) and Mars ($g = 0.3783$), which are relevant to future space exploration. For simplicity, we restrict attention to either small or large Ma. In long containers of $\Gamma \gg 1$, we note that g levels greater than 1 are used to cover a wider range of Bo_{dyn}.

The study is undertaken in two parts. First, we consider the direct effect of the gravity level on heat transport. Then, the transition from steady to oscillatory thermocapillary flow is located by decreasing Bo_{dyn}.

6.1. Heat transport

Figure 9 shows the enhancement factor $\mathcal{G}$ versus Bo_{dyn} for (a) Ma = 186224 and (b) Ma = 31037. The first set of simulations were performed by varying the gravity level g in fixed rectangular geometries of $\Gamma = 12$ (open squares) and $\Gamma = 1.5$ (solid squares). Generally, $\mathcal{G}$ increases as Bo_{dyn} is reduced and gravity becomes less important. For each choice of Ma and Γ, the enhancement factor for $\text{Bo}_{\text{dyn}} = 0$ (reproduced from Ref. [40]) is indicated with a thin horizontal coloured line. The asymptotic behaviour as $\text{Bo}_{\text{dyn}} \to 0$ is well-captured by those values. In the opposite limit of $\text{Bo}_{\text{dyn}} \gg 1$, natural convection is dominant over thermocapillary convection and $\mathcal{G} \to 1$.

Simulations also show that for $\text{Bo}_{\text{dyn}} < 2$ (marked with a thin vertical line), the thermocapillary effect *always* improves the average heat transfer rate during melting (i.e., $\mathcal{G} > 1$). This can be taken as a reference value for PCM design criteria. Note that, for a PCM of length $L = 22.5$ mm operating on the Moon, this criteria would require a PCM height $H < 14.9$ mm ($\Gamma > 1.51$) and, on Mars $H < 11.3$ mm ($\Gamma > 1.99$).

In addition to these simulations obtained by varying g, we include the results of Secs. 3 and 4, which were calculated for

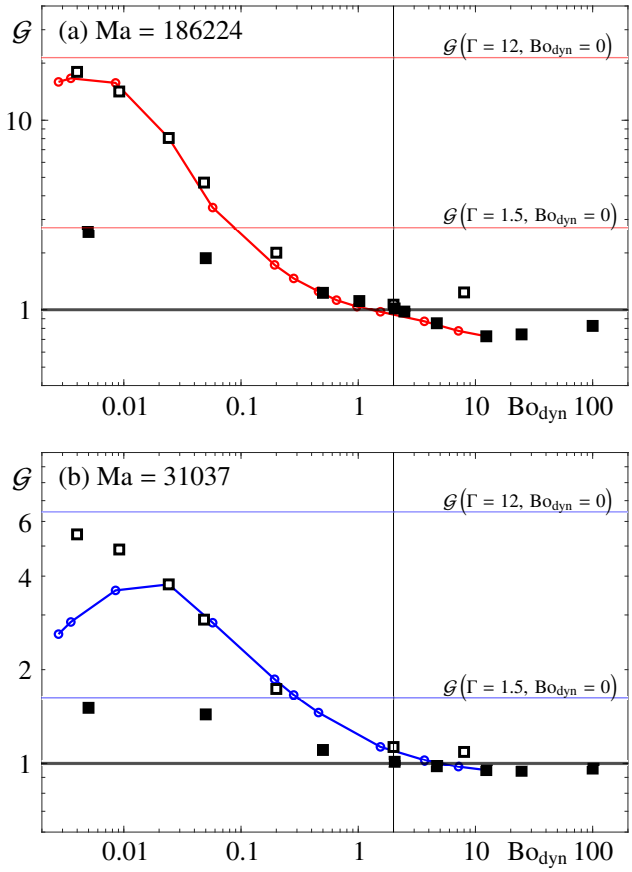

Figure 9: Enhancement factor $\mathcal{G}$ versus Bo_{dyn} for (a) Ma = 186224 and (b) Ma = 31037, calculated in two ways. The solid square markers correspond to $\Gamma = 1.5$ and $0.0004 \le g \le 8.08$, which covers the interval $0.005 \le \text{Bo}_{\text{dyn}} \le 100$. The open markers correspond to $\Gamma = 12$ and $0.165 \le g \le 331$, which covers the interval $0.004 \le \text{Bo}_{\text{dyn}} \le 8$. The red (blue) open circles correspond to simulations with fixed gravity $g = 1$ and $1.5 \le \Gamma \le 24.7$. Coloured horizontal lines indicate $\mathcal{G}$ in the microgravity limit ($\text{Bo}_{\text{dyn}} = 0$), reproduced from [40]. The black horizontal lines mark $\mathcal{G} = 1$. The vertical lines mark $\text{Bo}_{\text{dyn}} \approx 2$, beyond which $\mathcal{G} < 1$ (i.e., the thermocapillary effect delays melting).

$g = 1$ and various Γ. The different Γ values were obtained by changing the container height H with fixed L so that larger Γ implies smaller Bo_{dyn}; see Eq. (21). These curves match relatively well, over a wide range of Bo_{dyn}, with those obtained by varying g. The main discrepancy is for $\text{Bo}_{\text{dyn}} < 0.05$ in (b). For these parameters, H becomes comparable to the thickness of the viscous boundary layers, which increases damping and reduces convective heat transport, leading to a smaller enhancement factor $\mathcal{G}$.

The melting of n-octadecane in a square container (i.e., $\Gamma = 1$) was considered by Madruga and Mendoza [30] for different values of Bo_{dyn}. The thermocapillary effect was found to increases the average heat transfer rate by a factor of 1.39 for $\text{Bo}_{\text{dyn}} = 8.3$ and 1.07 for $\text{Bo}_{\text{dyn}} = 33$. However, these results were obtained with an adiabatic condition at the cold wall, which has a significant effect on the melting process, as discussed below.

During the early stages of melting, the low conductivity of the solid PCM acts to insulate the liquid and the process is not

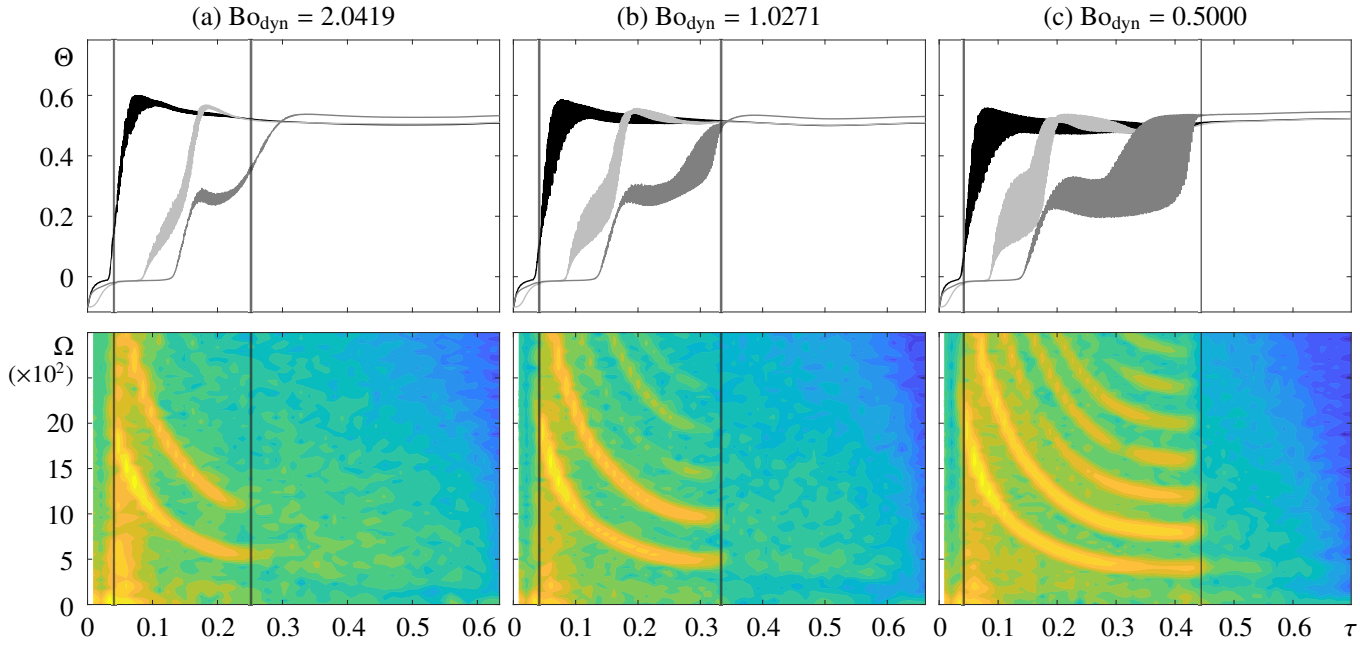

Figure 10: Dynamics of melting with mixed convection for Ma = 186224, Γ = 1.5 and three different dynamic Bond numbers: (a) $\mathrm{Bo}_{\mathrm{dyn}} = 2.0419$ ($g = 0.165$), (b) $\mathrm{Bo}_{\mathrm{dyn}} = 1.0271$ ($g = 0.083$), (c) $\mathrm{Bo}_{\mathrm{dyn}} = 0.5000$ ($g = 0.0404$). In the upper row, the time dependence of Θ for $0 \le \tau \le \tau_{\mathrm{melt}}$ is shown at three points located along $y = (3/4)\,\Gamma^{-1}$ at $x = 1/8$ (black), $1/2$ (light grey) and $7/8$ (dark grey). The lower row shows the corresponding spectrogram for the temperature deviation $\widehat{\Theta} = \Theta - \langle\Theta\rangle$ at $x = 1/2$. The vertical lines indicate the approximate extent of the oscillatory mode. Note that the spectrogram depends weakly on $\mathrm{Bo}_{\mathrm{dyn}}$. Frequencies are nondimensionalised with the thermal diffusion timescale L^2/α.

sensitive to the thermal boundary conditions at the cold wall. The thermocapillary effect accelerates melting in the vicinity of the liquid/air interface during this period. Once the solid/liquid front reaches the cold wall, however, the thermal boundary condition plays a crucial role in the subsequent development.

For the adiabatic boundary condition of Madruga and Mendoza [30], the heat transferred through the hot boundary continuously increases the temperature of the liquid and thereby reduces the temperature gradient along the thermocapillary surface. The thermocapillary convection is, therefore, progressively weakened and, after a sufficiently long time, the melting process is dominated by natural convection. Since thermocapillary convection enhances melting at earlier times and plays a diminishing role at later times (when the upward shift of the vortices described in Sec. 4 can reduce heat transfer), the overall enhancement factor with adiabatic boundary conditions is greater than unity.

With the constant temperature boundary condition used here, the cold wall acts to maintain a thermal gradient along the free surface, and also evacuates heat after the solid/liquid front reaches it. This heat loss and the sustained thermocapillary flow, which pulls the vortical structure upwards, are the two main factors that slow down melting at later times, sometimes making τ_{melt} larger than with natural convection alone. For the results presented above, it is the relative extension of this final stage compared to the total melting time that determines whether the presence of thermocapillary convection is beneficial or detrimental to the overall melting process. The relative importance of this final stage is controlled, to a large extent, by the container aspect ratio Γ. Note that the changes in this final stage are reminiscent of the distinction, mentioned above, between the investigations of Beckermann and Viskanta [19] and those of Wang et al. [20], even though those experiments considered only the effect of natural convection during the phase change.

6.2. *Oscillatory flow and critical Bond number*

As mentioned above, one of the most striking differences between the current results for $g = 1$ and those in microgravity is the (quasi-) steady nature of the flow across the full range of parameters considered. The prevalence of oscillatory flow in weightless conditions suggests that if gravity is continuously lowered from its normal value with fixed Ma, a transition to oscillatory flow will occur a some critical $\mathrm{Bo}_{\mathrm{dyn}}^{\mathrm{cr}}$.

Figure 10 illustrates the type of oscillatory dynamics observed below this transition with Ma = 186224, Γ = 1.5, and (a) $\mathrm{Bo}_{\mathrm{dyn}} = 2.0419$ ($g = 0.165$), (b) $\mathrm{Bo}_{\mathrm{dyn}} = 1.0271$ ($g = 0.083$), (c) $\mathrm{Bo}_{\mathrm{dyn}} = 0.5000$ ($g = 0.0404$). In each case, the upper panel shows the temperature $\Theta(\tau)$ measured at three points along $y = (3/4)\,\Gamma^{-1}$ at $x = 1/8$ (black), $1/2$ (light grey), and $7/8$ (dark grey). The lower panel shows the spectrogram corresponding to the temperature deviation $\widehat{\Theta} = \Theta - \langle\Theta\rangle$ at $x = 1/2$, where $\langle\Theta\rangle$ is the time average. Vertical lines mark the approximate period during which the oscillatory mode appears. Recall that the results presented in Sec. 4 for a higher value of $\mathrm{Bo}_{\mathrm{dyn}} = 12.375$ do not show oscillations.

As described in Ref. [39], oscillatory thermocapillary flow in small Γ containers features the OSW mode, which is char-

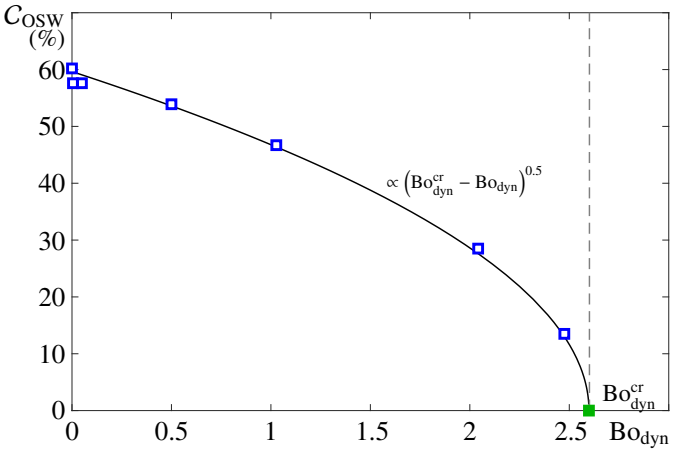

Figure 11: Contribution C_{OSW} of the OSW mode to the phase change for $\mathrm{Bo}_{\mathrm{dyn}} < 3$ with $\mathrm{Ma} = 186224$ and $\Gamma = 1.5$. The measurements (open blue squares) are fit (black solid curve) using a square-root scaling $(\mathrm{Bo}^{\mathrm{cr}}_{\mathrm{dyn}} - \mathrm{Bo}_{\mathrm{dyn}})^{0.5}$ to estimate $\mathrm{Bo}^{\mathrm{cr}}_{\mathrm{dyn}} = 2.5988$ (green marker; $g_{\mathrm{cr}} = 0.21$). For $g \to 0$, the contribution of the oscillatory mode agrees with the microgravity results of Ref. [39].

acterised by the cyclic pulsation of the main vortical structure. The pulsation frequency was found to diminish as the solid/liquid front progresses, and this was associated with a reduction in the number of vortices present. The lower panels of Fig. 10 reveal the same type of behaviour.

The variation of $\mathrm{Bo}_{\mathrm{dyn}}$ from 2.0419 in (a) to 0.5 in (c) results in an OSW mode that appears at (nearly) the same time but persists longer as $\mathrm{Bo}_{\mathrm{dyn}}$ is reduced. We follow Ref. [39] and use the oscillatory contribution

$$C_{\mathrm{OSW}} = \frac{\tau^{\mathrm{f}}_{\mathrm{osc}} - \tau^{0}_{\mathrm{osc}}}{\tau_{\mathrm{melt}}}\,, \tag{23}$$

to determine the critical value. Here, τ^{0}_{osc} and $\tau^{\mathrm{f}}_{\mathrm{osc}}$ denote the beginning and the end of the oscillations, respectively. The parameter C_{OSW} simply measures the fraction of the melting time where the OSW mode is present and, in this way, quantifies the contribution of oscillatory flow to the full melting process.

Figure 11 shows the calculated values (blue markers) of C_{OSW} for different $\mathrm{Bo}_{\mathrm{dyn}}$. These can be fit (solid line) using a square-root scaling $(\mathrm{Bo}^{\mathrm{cr}}_{\mathrm{dyn}} - \mathrm{Bo}_{\mathrm{dyn}})^{0.5}$, which allows for a straightforward estimate of $\mathrm{Bo}^{\mathrm{cr}}_{\mathrm{dyn}} = 2.5988$ ($g_{\mathrm{cr}} = 0.21$), which is shown with a green marker. We note that in the limit $\mathrm{Bo}_{\mathrm{dyn}} \to 0$, the contribution C_{OSW} agrees with the results of Salgado Sanchez et al. [39].

Figure 12 shows, for $\mathrm{Ma} = 186224$ and $\mathrm{Bo}_{\mathrm{dyn}} = 0.0121$ ($g = 0.5$), the type of oscillatory convection observed in a long container of $\Gamma = 12$. The upper panel shows the dimensionless temperature $\Theta(\tau)$ for $\tau \le \tau_{\mathrm{melt}}$ at three points located along $y = (2/3)\,\Gamma^{-1}$ at $x = 1/12$ (black), $1/2$ (light grey), and $11/12$ (dark grey). The spectrogram corresponding to the temperature deviation $\widetilde{\Theta} = \Theta - \langle\Theta\rangle$ at $x = 1/2$ is shown in the lower panel. A vertical line marks the appearance of oscillations.

As described in Ref. [39], the oscillatory flow observed during melting in long containers is characterised by the appearance of an HTW mode. This mode is associated with the repeated creation of vortices that travel inwards from the cold

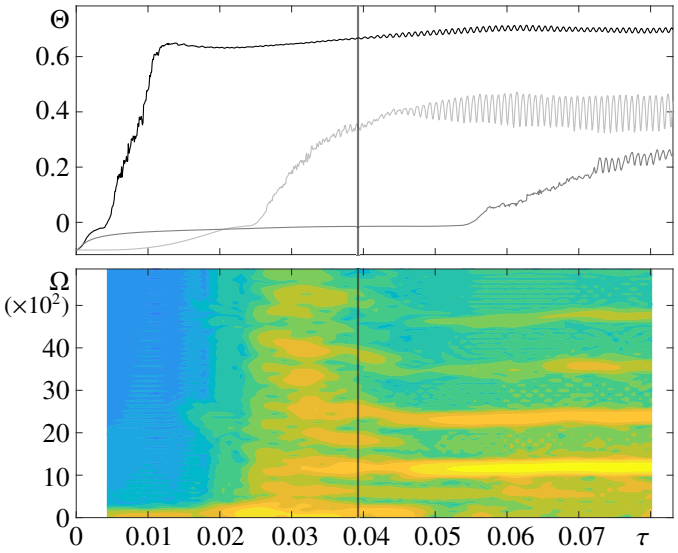

Figure 12: Dynamics of melting with mixed convection for $\mathrm{Ma} = 186224$, $\Gamma = 12$ and $\mathrm{Bo}_{\mathrm{dyn}} = 0.0121$ ($g = 0.5$). In the upper panel, the time dependence of Θ for $0 \le \tau \le \tau_{\mathrm{melt}}$ is shown at three points located along $y = (2/3)\,\Gamma^{-1}$ at $x = 1/12$ (black), $1/2$ (light grey) and $11/12$ (dark grey). The lower panel shows the corresponding spectrogram for the temperature deviation $\widetilde{\Theta} = \Theta - \langle\Theta\rangle$ at $x = 1/2$. The vertical line indicates, approximately, the appearance of the oscillatory mode. Frequencies are nondimensionalised with the thermal diffusion timescale L^2/α.

boundary. Their intensity decays as they travel, becoming negligible near the hot wall. The HTW frequency was found to be insensitive to Ma and to the progression of the solid/liquid front, consistent with the idea that the cold boundary region selects the oscillation frequency. The lower panel of Fig. 12 demonstrates this same type of behaviour, with a nearly constant dominant frequency (harmonics are present as well).

We define the HTW contribution following Ref. [39] as

$$C_{\mathrm{HTW}} = 1 - \frac{\tau^{0}_{\mathrm{osc}}}{\tau_{\mathrm{melt}}}\,, \tag{24}$$

to determine the critical value. Note that HTW modes generally persist beyond the completion of melting so that $\tau^{\mathrm{f}}_{\mathrm{osc}} = \tau_{\mathrm{melt}}$, which is assumed above.

The measured C_{HTW} values (red markers) are given in Fig. 13 for different $\mathrm{Bo}_{\mathrm{dyn}}$. These are fit (solid line) to a fourth-root scaling $(\mathrm{Bo}^{\mathrm{cr}}_{\mathrm{dyn}} - \mathrm{Bo}_{\mathrm{dyn}})^{0.25}$ to estimate $\mathrm{Bo}^{\mathrm{cr}}_{\mathrm{dyn}} = 0.0205$ ($g_{\mathrm{cr}} = 0.85$), which is shown with a green marker. As before, the limit $\mathrm{Bo}_{\mathrm{dyn}} \to 0$ is consistent with the results of Salgado Sanchez et al. [39], where more details of the oscillatory modes can be found.

7. Conclusions

This paper presents results from a numerical study of PCM melting under the combined effect of natural and thermocapillary convection in rectangular geometry. The substantial improvement in performance that may be obtained via the thermocapillary effect, even under normal gravity, suggests that PCM

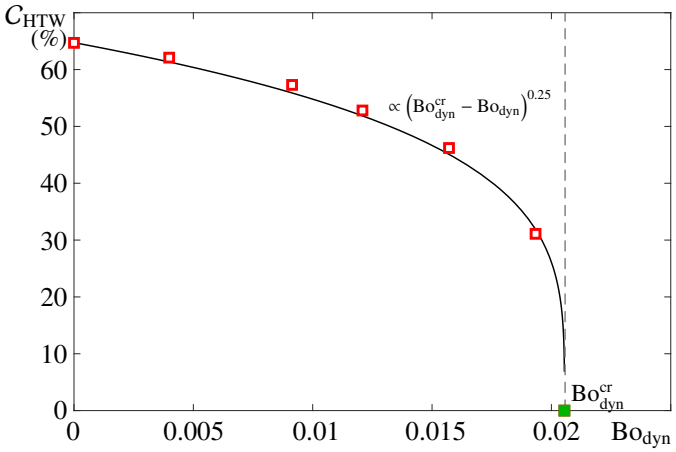

Figure 13: Contribution C_{HTW} of the HTW mode to the phase change for $\mathrm{Bo}_{\mathrm{dyn}} < 0.025$ with Ma = 186224 and $\Gamma = 1.5$. The measurements (open red circles) are fit (black solid curve) using a fourth-root scaling $(\mathrm{Bo}^{\mathrm{cr}}_{\mathrm{dyn}} - \mathrm{Bo}_{\mathrm{dyn}})^{0.25}$ to estimate $\mathrm{Bo}^{\mathrm{cr}}_{\mathrm{dyn}} = 0.0205$ (green marker; $g_{\mathrm{cr}} = 0.85$). For $g \to 0$, the contribution of the oscillatory mode agrees with the microgravity results of Ref. [39].

designs could benefit from this heat transport mechanism across a wide range of applications.

The phase change is described using an enthalpy-porosity formulation of the Navier–Stokes equations [43], which models the coexisting solid and liquid states as a single phase with physical properties that depend on temperature and change sharply across the solid/liquid front. The problem is studied for the case of n-octadecane, an alkane with high Prandtl number (Pr = 52.53), due to its relevance to recent experimental [32–34] and numerical investigations [39, 40].

The PCM is subjected to a controlled phase change transition by imposing isothermal conditions on the lateral walls. The advance of the solid/liquid front during melting leaves a free surface with a temperature gradient that supports thermocapillary flow in the liquid. This flow, together with that of natural convection, acts as a mechanism for heat transport and changes the dynamics of the phase change. The influence of key dimensionless parameters is analysed, including the container aspect ratio (Γ), which defines the geometry, the Rayleigh (Ra) and Marangoni (Ma) numbers, which quantify the strength of natural and thermocapillary convection, and their relative importance, which is characterised by the dynamic Bond number ($\mathrm{Bo}_{\mathrm{dyn}}$). To the best of our knowledge, the present work provides the first systematic analysis covering a wide range of these parameters.

In Sec. 3, the phase change process is first studied with only natural convection. The results are presented for two representative aspect ratios (12 and 1.5) and two applied temperatures (5 K and 30 K). In long shallow containers, Ra is small, as is the effect of natural convection. The melting in this case is characterised by a slightly faster progression of the solid/liquid front along the upper portion of the container and a single large vortex that extends throughout the liquid. In deep containers, Ra is larger (by several orders of magnitude for the same applied temperatures) and natural convection is correspondingly stronger, with a greater reduction in melting time. The flow is characterised by a single vortex at early times, which splits in two vortices at later times. The final structure is asymmetric, with these two vortices centred at approximately half the container height.

The thermocapillary effect is included in Sec. 4, with the same values of Γ and applied temperatures. For large Γ, the thermocapillary flow is qualitatively similar to that observed in microgravity conditions [39], since Ra is small and $\mathrm{Bo}_{\mathrm{dyn}} \ll 1$. The dynamics in the liquid evolves from the classical *steady return flow* (SRF) state to a *steady multicellular structure* (SMC) as Ma is increased.

In short containers, $\mathrm{Bo}_{\mathrm{dyn}}$ is larger and the effect of natural convection is amplified. Two stages of the melting process can be distinguished. In the beginning, melting is significantly accelerated in a thin layer near the thermocapillary surface, where the flow structure resembles the SMC mode typical of large Γ containers. As the solid/liquid front reaches the cold wall, the flow transitions to a state with two vortices located near the free surface. This vortex arrangement has the effect of delaying melting (compared to the case of pure natural convection) during the later stage, since the interaction of the vortical flow with the solid/liquid front diminishes.

The influence of thermocapillary convection on heat transport is quantitatively evaluated in Sec. 5 over a large range of parameters: $1.5 \leq \Gamma \leq 24.7$ and $\mathrm{Ma} \leq 248298$. The ratio of melting times with and without thermocapillary convection is used to define the enhancement factor $\mathcal{G} = \tau_{\mathrm{g}}/\tau_{\mathrm{g+Ma}}$. For $\Gamma \gg 1$, thermocapillary convection significantly accelerates the melting process, enhancing the average heat transfer rate of the system at large Ma by factors as large as 20. For $\Gamma \lesssim 8$, in contrast, there is relatively weak dependence on Ma of $\mathcal{G}$, which take values of approximately 1–3. The fact that PCM devices in this range of Γ have similar performance over a wide range of operating temperatures could be an advantage for some design criteria. Finally, for $\Gamma \lesssim 3$, the thermocapillary effect can compromise PCM performance, with enhancement factors $\mathcal{G} < 1$ (as mentioned, this is due to the proximity of the vortices to the thermocapillary surface during the final melting stage). Note, however, that heat transport is improved during the early melting stage, even in this case.

Finally, the influence of gravity is studied in Sec. 6 to explore its stabilising effect on the dynamics of the flow — no oscillatory convection is observed with normal gravity over the range of Ma considered. By reducing $\mathrm{Bo}_{\mathrm{dyn}}$, the transition to oscillatory dynamics is investigated. The threshold $\mathrm{Bo}^{\mathrm{cr}}_{\mathrm{dyn}}$ for oscillatory flow is determined for two representative aspect ratios. We find that the oscillatory flow has features similar to those observed in microgravity [39]. The *oscillatory standing wave* (OSW) mode has a time-dependent spectrum, with a dominant frequency that decreases as melting progresses. The spectrum of the *hydrothermal travelling wave* (HTW) mode, on the other hand, is largely insensitive to the changes in the liquid domain caused by the advancing solid/liquid front.

Declaration of Competing Interest

The authors report no conflict of interest.

Acknowledgements

This work was supported by the Spanish Support and Operations Centre (E-USOC) and the Escuela Técnica Superior de Ingeniería Aeronáutica y del Espacio at the Universidad Politécnica de Madrid. We thank, in particular, the research group of Ciencias y Operaciones Aeroespaciales for their invaluable efforts.

[1] N. Chaiyat, T. Kiatsiriroat, Energy reduction of building air-conditioner with phase change material in Thailand, Case Studies in Thermal Engineering 4 (2014) 175—-186.

[2] K. O. Lee, M. A. Medina, Using phase change materials for residential air conditioning peak demand reduction and energy conservation in coastal and transitional climates in the State of California, Energy and Buildings 116 (2016) 69–77.

[3] R. Kandasamy, X.-Q. Wang, A. S. Mujumdar, Application of phase change materials in thermal management of electronics, Applied Thermal Engineering 27 (2007) 2822–2832.

[4] J. Hu, K. M. Babu, Fabric Testing. Chapter 10 - Testing intelligent textiles, Woodhead Publishing Series in Textiles, 2008.

[5] B. Pause, Smart Textile Coatings and Laminates. Chapter 7 - Phase change materials and their applications in coating and laminates for textiles, The Textile Institute Book Series, 2019.

[6] M. Esen, T. Ayhan, Development of a model compatible with solar assisted cylindrical energy storage tank and variation of stored energy with time for different phase change materials, Energy Conversion and Management 37 (1996) 1775–1785.

[7] M. Esen, Thermal performance of a solar-aided latent heat storage used for space heating by heat pump, Solar Energy 69 (2000) 15–25.

[8] P. H. Biwole, P. Eclache, F. Kuznik, Phase change materials to improve solar panel's performace, Energy and Buildings 62 (2013) 59–67.

[9] C. J. Ho, B.-T. Jou, C.-M. Lai, C.-Y. Huang, Performance assessment of a BIPV integrated with a layer of water-saturated MEPCM, Energy and Buildings 67 (2013) 322–333.

[10] A. Sharma, V. V. Tyagi, C. R. Chen, D. Buddhi, Review on thermal energy storage with phase change materials and applications, Renewable and Sustainable Energy Reviews 13 (2009) 318–345.

[11] Y. B. Tao, Y.-L. He, A review of phase change material and performance enhancement method for latent heat storage system, Renewable and Sustainable Energy Reviews 93 (2018) 245–259.

[12] C. Gau, R. Viskanta, Melting and Solidification of a Pure Metal on a Vertical Wall, Transactions of the ASME 108 (1986) 174–181.

[13] A. D. B. an V. R. Voller, K. J. Reid, Enthalpy-porosity technique for modelling convection-diffusion phase change: application to the melting of a pure metal, Numerical Heat Transfer 13.

[14] S. K. Roy, S. Sengupta, Gravity-assisted melting in a spherical enclosure: effects of natural convection, International Journal of Heat and Mass Transfer 33 (1990) 1135–1147.

[15] J. M. Khodadadi, Y. Zhang, Effects of buoyancy-driven convection on melting within spherical containers, International Journal of Heat and Mass Transfer 44 (2001) 1605–1618.

[16] S. Wang, A. Faghri, T. L. Bergman, A comprehensive numerical model for melting with natural convection, International Journal of Heat and Mass Transfer 53 (2010) 1986–2000.

[17] A. Joulin, Z. Younsi, L. Zalewski, S. Lassue, D. R. Rousse, J.-P. Cavrot, Experimental and numerical investigation of a phase change material: thermal-energy storage and release, Applied Energy 88 (2011) 2454–2462.

[18] H. Shokouhmand, B. Kamkari, Experimental investigation on melting heat transfer characteristics of lauric acid in a rectangular thermal storage unit, Experimental Thermal and Fluid Science 50 (2013) 201–212.

[19] C. Beckermann, R. Viskanta, Effect of solid subcooling on natural convection melting of a pure metal, Journal of Heat Transfer 111 (1989) 414–424.

[20] Y. Wang, A. Amiri, K. Vafai, An experimental investigation of the melting process in a rectangular enclosure, International Journal of Heat and Mass Transfer 42 (1999) 3659–3672.

[21] D. Yanxia, Y. Yanping, J. Daiyong, C. Baoyi, M. Jinfeng, Experimental investigation on melting characteristics of ethanolamine–water binary mixture used as PCM, International Communications in Heat and Mass Transfer 34 (2007) 1056–1063.

[22] N. S. Dhaidan, J. M. Khodadadi, Melting and convection of phase change materials in different shape containers: A review, Renewable and Sustainable Energy Reviews 43 (2015) 449–477.

[23] Z.-X. Gong, S. Devahastin, A. S. Mujumdar, Enhanced heat transfer in free convection-dominated melting in a rectangular cavity with an isothermal vertical wall, Applied Thermal Engineering 19 (1999) 1237–1251.

[24] H. M. Ettouney, I. Alatiqi, M. Al-Sahali, S. A. Al-Ali, Heat transfer enhancement by metal screens and metal spheres in phase change energy storage systems, Renewable Energy 29 (2004) 841–860.

[25] F. Agyenim, P. Eames, M. Smyth, A comparison of heat transfer enhancement in a medium temperature thermal energy storage heat exchanger using fins, Solar Energy 83 (2009) 1509–1520.

[26] D. Fernandes, F. Pitie, G. Caceres, J. Baeyens, Thermal energy storage: "How previous findings determine current research priorities", Energy 39 (2012) 246–257.

[27] A. Atal, Y. Wang, M. Harsha, S. Sengupta, Effect of porosity of conducting matrix on a phase change energy storage device, Journal of Heat and Mass Transfer 93 (2016) 9–16.

[28] S. F. Hosseinizadeh, A. A. R. Darzi, F. L. Tan, Numerical investigations of unconstrained melting of nano-enhanced phase change material (NEPCM) inside a spherical container, International Journal of Thermal Sciences 51 (2012) 77–83.

[29] N. S. Dhaidan, J. M. Khodadadi, T. A. Al-Hattab, S. M. Al-Mashat, Experimental and numerical investigation of melting of NePCM inside an annular container under a constant heat flux including the effect of eccentricity, International Journal of Heat and Mass Transfer 67 (2013) 455–468.

[30] S. Madruga, C. Mendoza, Enhancement of heat transfer rate on phase change materials with thermocapillary flows, European Physical Journal Special Topics 226 (2017) 1169–1176.

[31] S. Madruga, C. Mendoza, Heat transfer performance and melting dynamic of a phase change material subjected to thermocapillary effects, International Journal of Heat and Mass Transfer 109 (2017) 501–510.

[32] J. M. Ezquerro, A. Bello, P. Salgado Sanchez, A. Laveron-Simavilla, V. Lapuerta, The Thermocapillary Effects in Phase Change Materials in Microgravity experiment: design, preparation and execution of a parabolic flight experiment, Acta Astronautica 162 (2019) 185–196.

[33] J. M. Ezquerro, P. Salgado Sanchez, A. Bello, J. Rodriguez, V. Lapuerta, A. Laveron-Simavilla, Experimental evidence of thermocapillarity in Phase Change Materials in microgravity: measuring the effect of Marangoni convection in solid/liquid phase transitions, International Communications of Heat and Mass Transfer 113 (2020) 104529.

[34] P. Salgado Sanchez, J. M. Ezquerro, J. Porter, J. Fernandez, I. Tinao, Effect of thermocapillary convection on the melting of Phase Change Materials in microgravity: experiments and simulations, International Journal of Heat and Mass Transfer 154 (2020) 119717.

[35] W. R. Humphries, E. I. Griggs, A design handbook for phase change thermal control and energy storage devices, Tech. Rep., NASA, 1977.

[36] M. Giangi, F. Stella, E. Leonardi, G. De Vahl Davis, A numerical study of solidification in the presence of a free surface under microgravity conditions, Numerical Heat Transfer Part A: Applications 57 (2002) 457–473.

[37] T. D. Swanson, G. C. Birur, NASA thermal control technologies for robotic spacecraft, Applied Thermal Engineering 23 (2003) 1055–1065.

[38] G. Xiaohong, S. Xiange, Z. Miao, T. Dawei, Influence of void ratio on thermal stress of PCM canister for heat pipe receiver, Applied Thermal Engineering 94 (2012) 615–621.

[39] P. Salgado Sanchez, J. M. Ezquerro, J. Fernandez, J. Rodriguez, Thermocapillary effects during the melting of Phase Change Materials in microgravity: steady and oscillatory flow regimes, Journal of Fluid Mechanics 908 (2021) A20.

[40] P. Salgado Sanchez, J. M. Ezquerro, J. Fernandez, J. Rodriguez, Thermocapillary effects during the melting of phase change materials in microgravity: heat transport enhancement, International Journal of Heat and Mass transfer 163 (2020) 120478.

[41] L. D. Landau, E. M. Lifshitz, Fluid Mechanics, Pergamon books Ltd., 1987.

[42] P. W. Egolf, H. Manz, Theory and modeling of phase change materials with and without mushy regions, International Journal of Heat and Mass Transfer 37 (1994) 2917–2924.

[43] V. R. Voller, M. Cross, N. C. Markatos, An enthalpy method for convection/diffusion phase change, International Journal for Numerical Methods in Engineering 24 (1987) 271–284.
[44] J. M. Montanero, C. Ferrero, V. M. Shevtsova, Experimental study of the free surface deformation due to thermal convection in liquid bridges, Experiments and Fluids 45 (2008) 1087–1101.
[45] V. Shevtsova, A. Mialdun, C. Ferrera, M. Ermakov, M. G. Cabezas, J. Montanero, Subcritical and Oscillatory Dynamic Surface Deformations in Non-Cylindrical Liquid Bridges, Fluid Dynamics and Material Processing 4 (2008) 43–54.
[46] M. K. Smith, S. H. Davis, Instabilities of dynamic thermocapillary liquid layers. Part 1. Convective instabilities, Journal of Fluid Mechanics 132 (1983) 119–144.
[47] L. J. Peltier, S. Biringen, Time-dependent thermocapillary convection in a rectangular cavity: numerical results for a moderate Prandtl number fluid, Journal of Fluid Mechanics 257 (1993) 339–357.
[48] H. C. Kuhlmann, S. Albensoeder, Three-dimensional flow instabilities in a thermocapillary-driven cavity, Physical Review E 77 (2008) 036303.
[49] I. Harari, T. Hughes, What are C and h?: Inequalities for the analysis and design of finite element methods, Computer Methods in Applied Mechanics and Engineering 97 (1992) 157–192.
[50] R. Codina, A discontinuity-capturing crosswind-dissipation for the finite element solution of the convection-diffusion equation, Computer Methods in Applied Mechanics and Engineering 110 (1993) 325–342.
[51] A. K. Sen, S. H. Davis, Steady thermocapillary flows in two-dimensional slots, Journal of Fluid Mechanics 121 (1982) 163–186.
[52] V. Shevtsova, A. Nepomnyashchy, J. C. Legros, Thermocapillary-buoyancy convection in a shallow cavity heated from the side, Physical Review E 67 (2003) 066308.
[53] P. Salgado Sanchez, J. M. Ezquerro, J. Porter, J. Fernandez, J. Rodriguez, I. Tinao, V. Lapuerta, A. Laveron-Simavilla, X. Ruiz, F. Gavalda, M. M. Mounir Bou-Ali, J. Ortiz, The effect of thermocapillary convection on PCM melting in microgravity: results and expectations, Advances in Astronautics Science and Technology, under review .